



Journal Name

ARTICLE

A Self-Assembly Toolbox for Thiophene-Based Conjugated Polyelectrolytes: Surfactants, Solvent and Copolymerisation

Judith E. Houston,^{*a} Michèle Chevrier,^b Marie-Sousai Appavou,^a Stephen M. King,^c Sébastien Clément^{*b} and Rachel C. Evans^{*d}

Received 00th January 20xx,
Accepted 00th January 20xx

DOI: 10.1039/x0xx00000x

www.rsc.org/

Targeted control of the aggregation, morphology and optical properties of conjugated polymers is critical for the development of high performance optoelectronic devices. Here, self-assembly approaches are used to strategically manipulate the order, conformation and spatial distribution of conjugated polymers in solution and subsequently prepared thin films. The supramolecular complex organisation of phosphonium-functionalised homo- (**P3HTPMe₃**) and diblock (**P3HT-*b*-P3HTPMe₃**) ionic conjugated polythiophenes upon solvent-mediation and co-assembly with oppositely charged surfactants is investigated. UV/Vis absorption and photoluminescence spectroscopies, small-angle neutron scattering (SANS), cryo-transmission electron microscopy (cryo-TEM) and atomic force microscopy (AFM) are used to probe the organisation and photophysical response of the aggregates formed. Subtle differences in the surfactant mole fraction and structure, as well as the solvent polarity, yield differences in the nature of the resultant homopolyelectrolyte-surfactant complexes. In contrast, only moderate structural transformations are observed for the amphiphilic diblock copolyelectrolyte, emphasising the structure “anchoring” effect of a neutral polymer block when amphiphilic copolymers are dissolved in polar solvents. These results highlight the versatility of self-assembly to access a range of nanomorphologies, which could be crucial for the design of the next generation of organic optoelectronic devices.

Introduction

Conjugated polyelectrolytes (CPEs) are polymers with extended π -conjugated backbones and ionic pendant groups, which combine organic semiconductor properties and the charge-mediated behaviour of polyelectrolytes in a single functional macromolecule.¹ They have remarkable promise as components of the active and charge transport layers of flexible optoelectronic devices, including polymer light-emitting diodes,²⁻⁴ organic field-effect transistors⁵⁻⁷ and organic photovoltaic devices (OPVs).⁸⁻¹¹ Inkjet or screen-printing provide a facile route to low cost fabrication of these devices.¹²⁻¹⁴ However, the nanostructure of CPE films deposited in this manner are strongly influenced by the conformation of the polymer species in the ink. Since device

performance depends on the intrinsically linked optoelectronic properties and nanoscale morphology of the polymer,¹⁵ the development of facile and reproducible processing methods that enable sophisticated control of the organisation of individual and clustered polymer chains in solution is paramount for the design of high performance organic electronic devices.

Recently, self-assembly strategies have emerged as an elegant approach for the fabrication of reproducible nanoscale architectures from CPEs.¹⁶ Due to their inherently amphiphilic structures (hydrophobic backbones and hydrophilic side groups), CPEs have a tendency to aggregate in aqueous solution or polar organic solvents, and as a result their aggregated morphology can be strongly dependent on the polarity of the medium.^{17, 18} The addition of ionic or neutral surfactants to aqueous solutions of CPEs is known to break-up these aggregates, leading to the formation of hybrid structures with well-defined organisation.¹⁹⁻²³ Such structural transitions result in concomitant changes in the photophysical properties, such as an increase in the emission intensity,^{24, 25} or a shift of the emission maximum.²⁶

Differences in the solubility and/or crystallinity of the polymer structure may also be exploited to yield more exotic structures. Block copolymers are macromolecules formed from two (or more) immiscible homopolymer chains (blocks) that are covalently linked. Due to the thermodynamic incompatibility between the adjacent blocks, these materials exhibit a natural tendency to self-assemble into

^a Jülich Centre for Neutron Science (JCNS) at Heinz Maier-Leibnitz Zentrum (MLZ), Forschungszentrum Jülich GmbH, Lichtenbergstr. 1, 85748 Garching, Germany. Email: j.houston@fz-juelich.de

^b Institut Charles Gerhardt – UMR 5253, Université de Montpellier – CC1701, Place Eugène Bataillon, F-34095 Montpellier Cedex 05, France. Email: sebastien.clement1@umontpellier.fr

^c ISIS Facility, STFC Rutherford Appleton Laboratory, Harwell Campus, Didcot, Oxon, OX11 0QX, United Kingdom.

^d Department of Materials Science & Metallurgy, University of Cambridge, 27 Charles Babbage Road, Cambridge, CB3 0FS, United Kingdom. Email: rce26@cam.ac.uk

† Footnotes relating to the title and/or authors should appear here.

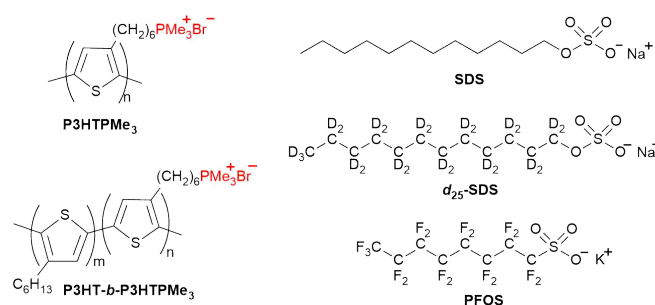
Electronic Supplementary Information (ESI) available: UV/Vis absorption and fluorescence spectra, SANS data analysis, cryo-TEM and AFM images. See DOI: 10.1039/x0xx00000x

nanodomains.²⁷ The shape and size of the nanostructured morphologies are determined by the chain stiffness, molecular weight, solubility of the individual blocks and block ratio.²⁸ Recently, particular attention has been paid to all-conjugated amphiphilic diblock copolymers, which combine ionic and neutral blocks.^{29, 30} This introduces a further solubility gradient across the copolymer structure, leading to exotic self-assembled structures that can be conveniently modulated *via* solvent-mediation. Scherf *et al.* reported all-conjugated cationic “rod-rod” block copolyelectrolytes containing a hydrophobic polyfluorene and hydrophilic polythiophene blocks, that exhibit solvent-mediated self-assembly in mixtures of selective and non-selective solvents, such as water-methanol^{30, 31} and water-THF.^{31, 32} Careful selection of the solvent mixture was shown to be a convenient method to simultaneously control the nanomorphology of the self-assembled aggregates formed (*e.g.* vesicles, rods, *etc.*) and the photoluminescence properties.³⁰⁻³²

All-conjugated polythiophenes have attracted particular attention for applications as electron donors or interfacial layer materials in OPV devices.³³⁻³⁹ The analogous amphiphilic diblock polythiophene copolymers should be extremely attractive for this purpose; however, to date, there have only been a few studies dedicated to controlling the aggregate morphology and thus optoelectronic properties of amphiphilic diblock polythiophene copolymers.^{29, 35, 40, 41} We recently reported the solvent-driven assembly of a family of rod-rod diblock copolymers containing a hydrophobic poly(3-hexylthiophene) (P3HT) block and a hydrophilic cationic P3HT block bearing different side-chains.²⁹ The rigid rod-structure led to the formation of core-shell cylindrical or disc-like aggregates in different solvent mixtures.²⁹ This investigation was followed by preliminary study of the interaction between the phosphonium-functionalised diblock copolymer poly[(3-hexylthiophene-2,5-diyl)]-*block*-poly[(3-(6’-(trimethylphosphoniumhexyl)thiophene-2,5-diyl))] bromide (**P3HT-*b*-P3HTPMe₃**), its analogous homopolyelectrolyte poly[3-(6’-(trimethylphosphonium)hexylthiophene-2,5-diyl)] bromide (**P3HTPMe₃**) (Scheme 1) and the anionic surfactant sodium dodecyl sulfate (SDS) in methanol-water mixtures. Small-angle neutron scattering (SANS) studies revealed that the solution structures, solvent content, and therefore hydrophobicity, were extremely dependent on both the CPE structure and counterion.³⁵ Furthermore, a 20% increase in power conversion efficiency of an OPV device was observed after the incorporation of the CPE-surfactant complexes as cathodic interfacial layers.³⁵

Here, we aim to comprehensively demonstrate the versatility of self-assembly to control the nanoscale morphology of all-conjugated homo- and diblock-polythiophene CPEs by harnessing solvent-mediation and co-assembly with ionic surfactants. The electrostatic co-assembly of the diblock copolymer **P3HT-*b*-P3HTPMe₃** and the analogous homopolymer **P3HTPMe₃** with the anionic surfactants, SDS, potassium heptadecafluoro-1-octanesulfonate (PFOS) and deuterated-sodium dodecyl sulfate (*d*₂₅-SDS) (Scheme 1) in both water and methanol is

investigated, and correlated with the nanoscale morphology of subsequently prepared thin films. Using a combination of optical, scattering and microscopic techniques, the nature of the homopolyelectrolyte-surfactant complexes is shown to be dependent on subtle differences in the surfactant mole fraction and structure, as well as the solvent polarity. In contrast, only moderate structural transformations are observed for the diblock **P3HT-*b*-P3HTPMe₃**, highlighting the “structure anchoring” effect of the neutral polymer block when amphiphilic copolymers are dissolved in polar solvents.



Scheme 1. Structures of the polythiophenes, **P3HTPMe₃** and **P3HT-*b*-P3HTPMe₃**, and surfactants, SDS, PFOS and *d*₂₅-SDS, used in this study.

Experimental

Materials and characterisation methods

Poly[3-(6’-(trimethylphosphonium)hexylthiophene-2,5-diyl)] bromide (**P3HTPMe₃**),⁴² and poly[(3-hexylthiophene-2,5-diyl)]-*block*-poly[(3-(6’-(trimethylphosphoniumhexyl)thiophene-2,5-diyl))] bromide (**P3HT-*b*-P3HTPMe₃**)³⁵ were synthesised as previously reported and have number-averaged molecular weights, M_n , of 15,100 and 13,600 g mol⁻¹, respectively, with PDIs of 1.12 and 1.36, as measured for the parent bromohexyl precursors.

SDS (≥99.0%), PFOS (≥98.0%) and deuterated-methanol (*d*₄-MeOD, 98.0%) were purchased from Sigma-Aldrich. Deuterated-sodium dodecyl sulfate (*d*₂₅-SDS) was purchased from Santa Cruz Biotechnology and deuterium oxide (D₂O, 99.9%) was purchased from Apollo Scientific Limited. All chemicals were used as received.

The UV/Vis absorption and fluorescence spectra were recorded at room temperature on a Shimadzu UV2401 PC UV/Vis scanning spectrometer and a Fluorolog-3 (Horiba Jobin Yvon) spectrophotometer, respectively. The emission spectra were corrected for the wavelength response of the system using correction factors supplied by the manufacturer. Samples were measured in quartz cells with an extremely short path length (0.1 mm) to prevent saturation of the detector signal.

SANS was carried out on the LOQ small-angle diffractometer at the ISIS Pulsed Neutron Source (STFC Rutherford Appleton Laboratory, Didcot, U.K.).⁴³ A simultaneous *q*-range of ~0.09–2.4 nm⁻¹ was achieved utilising an incident wavelength range of 0.22–1.0 nm separated by time-of-flight and employing a fixed sample-detector distance

of 4.1 m. $q = (4\pi/\lambda)\sin(\theta/2)$ where λ is the wavelength and θ the scattering angle. Samples were prepared in deuterated solvents to provide good neutron scattering contrast. The samples were placed in quartz cuvettes (Hellma) of 1 mm path length and maintained at 25.0 ± 0.5 °C. Each raw scattering data set was corrected for the detector efficiencies, sample transmission and background scattering and converted to scattering cross-section data ($d\Sigma/d\Omega$ vs. q) using the instrument-specific software.⁴⁴ These data were placed on an absolute scale (cm^{-1}) using the scattering from a standard sample (a solid blend of hydrogenated and perdeuterated polystyrene) in accordance with established procedures.⁴⁵ The scattering functions were fit using non-linear least-squares analysis to a Rigid Cylinder model,^{46,47} Lamellar Sheet model^{48,49} or a Core-Shell Cylinder model⁵⁰ using the SasView program (version 3.1.2).⁵¹ Full details of the models and the fitting procedure can be found in the Electronic Supplementary Information (ESI†).

Cryogenic-transmission electron microscopy (cryo-TEM) was performed at the Heinz Maier Leibnitz Zentrum, Garching, Germany. Cryo-TEM measurements were carried out on concentrated samples (10 mg mL^{-1} in D_2O). A copper grid coated with holey carbon film (Multi A, Quantifoil Micro Tools GmbH) was dipped in solution and then placed in the chamber of a cryo-plunge (EMGP Leica GmbH) maintained at 20 °C and 80% relative humidity (r.h.) The excess liquid was removed with filter paper. The samples were then cryo-fixed by rapid immersion into liquid ethane at -180 °C in the cryo-plunge. The specimens were inserted into a cryo-transfer holder (G910, Gatan, Munich, Germany) and transferred to a JEM 2200 FS EFTEM instrument (JEOL, Tokyo, Japan). Examinations were carried out at approximately -179 °C. The TEM was operated at an accelerating voltage of 200 kV. Zero-loss filtered images were taken under reduced dose conditions ($<10,000 \text{ e}^- \text{ nm}^{-2}$). All images were recorded digitally by a bottom-mounted 16 bit CCD camera system (TemCam-F216, TVIPS, Munich, Germany). The observable length scale range was between 5 and 500 nm.

Atomic force microscopy (AFM) measurements were performed using an Asylum Research MFP-3D™ instrument mounted on an anti-vibration plinth, in the tapping mode at room temperature under ambient conditions. Higher resolution AFM measurements were performed using diamond tips on silicon cantilevers, which were a kind gift from Adama Innovations. The silicon cantilevers had a spring constant of $\sim 110 \text{ nN nm}^{-1}$ and resonance frequency of $\sim 240 \text{ kHz}$. All raw AFM images were analysed using the Gwyddion 2.31 software.

Results and discussion

CPE-surfactant mixtures were prepared over a range of charge ratios, x , which represents the ratio of surfactant molecules over the number of charged CPE monomers. The samples were prepared by mixing 10 mg mL^{-1} solutions of CPE with 10 mg mL^{-1} solutions of surfactant to obtain the desired charge ratio, with a total concentration of 10 mg mL^{-1} . The value $x = 1$ corresponds to stoichiometric charge balance. As a

representative example, the compositions of polymer-SDS mixtures are given in the ESI†, Tables S1 and S2.

Optical characterisation

The optical properties of polythiophenes are well-known to be responsive to intrachain conformational changes and interchain aggregation.^{52, 53} The addition of the anionic surfactant SDS to a solution of **P3HTPMe₃** in D_2O at different charge ratios, x , resulted in a series of colorimetric transitions, as shown in Fig. 1. **P3HTPMe₃(SDS)_x** exhibits a series of well-defined colour transitions, from red ($x = 0$), to wine ($x = 1/5 - 1$), to orange ($x = 5$), and finally, yellow ($x = 20$). A similar series of colorimetric transitions for the related poly[3-(6'-(*N,N,N*-trimethylammoniumhexyl)thiophene-2,5-diyl)] bromide (**P3TMAHT**) with SDS at different charge ratios.²¹ In contrast, for **P3HT-*b*-P3HTPMe₃(SDS)_x** a colour transition from purple to red is only observed for $x = 5$ to $x = 20$.²¹

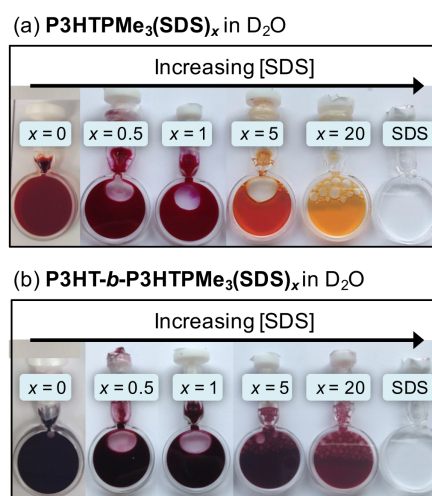


Figure 1. Photographs of (a) **P3HTPMe₃(SDS)_x**, and (b) **P3HT-*b*-P3HTPMe₃(SDS)_x**, as a function of charge ratio, x , in D_2O at room temperature (total conc. = 10 mg mL^{-1})

Effect of surfactant charge ratio. The colorimetric response can be correlated with changes in the UV/Vis absorption spectrum (Fig. 2a,b). The absorption spectra of **P3HTPMe₃(SDS)_x** exhibit similarly pronounced spectral transitions, where the absorption maximum (λ_{abs}) initially undergoes a red-shift from 443 nm ($x = 0$) to 545 nm ($x = 0.5$). Upon increasing the SDS charge ratio, a further red-shift is accompanied by the resolution of vibronic structure at the charge compensation point ($x = 1 - 2$). This is followed by a blue-shift to 429 nm for $x > 2$. The absorption maximum of the diblock copolymer **P3HT-*b*-P3HTPMe₃** is significantly red-shifted ($\sim 80 \text{ nm}$) compared to the homopolymer, which is consistent with its increased aggregation.²⁹ The λ_{abs} maxima remain relatively constant for the **P3HT-*b*-P3HTPMe₃(SDS)_x** series; however, there is a significant reduction in the absorption bandwidth with increasing x . By $x = 5$, the absorption band of **P3HT-*b*-P3HTPMe₃** also exhibits moderate vibronic structure, which is consistent with P3HT adopting a “rigid-rod” conformation in block copolymers.⁵⁴ Upon dilution of both of CPE-SDS systems by a factor of 100 (total

concentration = 0.1 mg mL⁻¹), the UV/Vis absorption spectra exhibit comparable trends to the concentrated samples (Fig. S1, ESI[†]). However, **P3HT-*b*-P3HTPMe₃** has a significantly narrower bandwidth in the diluted sample as the CPE is less aggregated at this concentration.

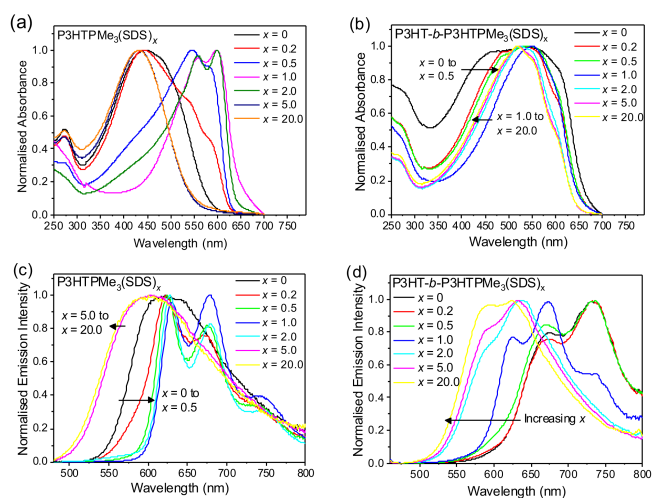


Figure 2. Effect of the surfactant charge fraction, x , on the optical properties of CPE-SDS _{x} complexes. (a,b) Normalised UV/Vis absorption spectra and (c,d) steady-state emission spectra for **P3HTPMe₃(SDS) _{x}** and **P3HT-*b*-P3HTPMe₃(SDS) _{x}** at room temperature. Total sample concentrations were 10 mg mL⁻¹ in D₂O. $\lambda_{\text{ex}} = 450$ nm.

The photoluminescence (PL) properties of the homopolymer and diblock copolymers are also highly sensitive to the surfactant charge ratio. Addition of SDS ($x = 0.2$ – 2) to **P3HTPMe₃** triggers both a narrowing of the emission band and the emergence of more resolved vibronic structure (Fig. 2c), which is assigned to the vibronic progression of the C=C stretching mode ($\Delta E \approx 0.15$ eV).⁵⁵ This is accompanied by a significant red-shift in the emission maximum ($\Delta\lambda_{\text{em}} = 59$ nm) by $x = 1$. These observations suggest that **P3HTPMe₃** adopts a more planar, ordered conformation in this concentration regime, which prevents free rotation around the polymer backbone.^{21, 22} By $x = 5$, the emission band loses its vibronic structure, broadens and undergoes a blue-shift, which indicate the return to a more twisted conformation along the polymer backbone.^{21, 22} In fact, the emission maximum for $x = 5$ is even blue-shifted when compared to that of pure **P3HTPMe₃**. This can be attributed to a reduction of interchain interactions due to increased screening of the polymer-polymer interactions by the SDS which is present in charge excess.^{21, 22}

The PL spectrum of **P3HT-*b*-P3HTPMe₃** has an emission maximum at 734 nm and some vibronic structure (Fig. 2d). Upon initial addition of SDS ($x = 0.2$ – 0.5), no significant spectral changes are observed, suggesting that no substantial structural reorganisation takes place in this concentration regime. However, for $x = 1$, a large blue-shift in the emission maximum to 672 nm results, which is accompanied by a decrease in the vibronic band at 734 nm and the emergence of a new band at 637 nm. Increasing the charge ratio further ($x = 2$ – 20) sees the complete loss of vibronic structure. The addition of the surfactant appears to reduce polymer-polymer

interactions.²³ The anionic surfactant is expected to associate predominantly through electrostatic interactions with the cationic **P3HTPMe₃** block, while polymer-polymer interactions are expected to persist in the neutral **P3HT** block domains of the copolymer aggregates. This may explain why some vibronic structure remains until $x = 5$, *i.e.* even when the surfactant is present in large excess.

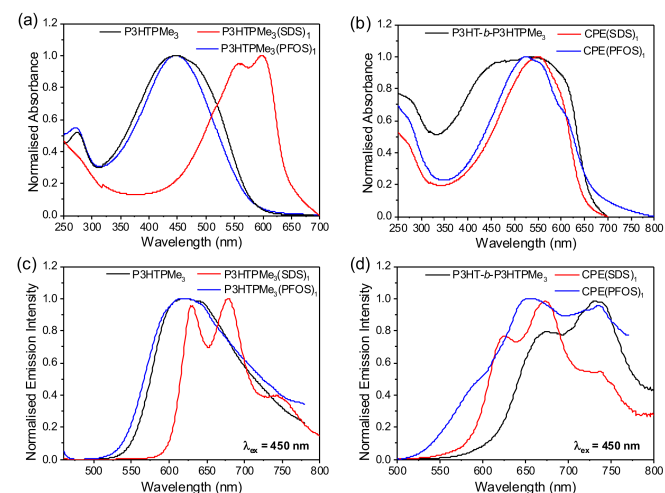


Figure 3. Effect of hydrogenated vs. perfluorinated surfactants on the optical properties of CPE-SDS _{x} complexes. Normalised UV/Vis absorption and emission spectra for (a,c) **P3HTPMe₃** and (b,d) **P3HT-*b*-P3HTPMe₃** with no surfactant (black lines) and 1:1 charge ratio of SDS (red lines) or PFOS (blue lines) at room temperature. Total sample concentrations were 10 mg mL⁻¹ in D₂O. $\lambda_{\text{ex}} = 450$ nm.

Effect of hydrogenated vs. perfluorinated surfactant. While a previous study has suggested that the nature of the cationic side-group (X) did not have a large effect on the self-assembly properties of **P3HT-*b*-P3HTX** in MeOH and H₂O,²⁹ it has been shown that subtle changes in the structure of the associating surfactant can tune the aggregate structures formed.²¹⁻²³ To investigate this, **P3HT-*b*-P3HTPMe₃** and **P3HTPMe₃**, were mixed with the perfluorinated surfactant, PFOS (Scheme 1). PFOS has a reduced charge density on the head-group and a more rigid hydrophobic tail in comparison to SDS.^{56, 57} The normalised UV/Vis absorption and PL spectra of the polythiophenes mixed with a 1:1 charge ratio of PFOS and, for comparison, SDS, are shown in Figure 3. The normalised PL spectra of **P3HTPMe₃(PFOS) _{x}** and **P3HT-*b*-P3HTPMe₃(PFOS) _{x}** ($x = 0.2$ - 5) are shown in Figure S2, ESI[†].

The UV/Vis absorption spectra for **P3HTPMe₃(PFOS)₁** and **P3HT-*b*-P3HTPMe₃(PFOS)₁** are characterised by a single broad absorption band centred at 447 and 523 nm, respectively (Fig. 3a,b), similar to the spectra for the pure CPEs. The only significant difference is a reduction in the peak width for **P3HT-*b*-P3HTPMe₃(PFOS)₁**. This is in stark contrast to the analogous SDS systems which are significantly red-shifted upon complexation with the surfactant.

The PL spectrum of **P3HTPMe₃** is notably insensitive to PFOS, with only a moderate blue-shift observed ($\Delta\lambda_{\text{em}} = 33$ nm) by $x = 2$, before a red-shift back to the original emission maximum at higher x . In contrast, the PL spectrum of **P3HT-*b*-P3HTPMe₃** undergoes a large blue-shift (~ 75 nm) to 657 nm by

$x = 1$. By $x = 5$, $\lambda_{em} = 614$ nm, and all vibronic structure is lost. This occurs for PFOS at a lower charge ratio ($x = 2$) than with SDS ($x = 5$), which suggests that the fluorinated surfactant, with a lower head-group charge density, is more effective at reducing polymer-polymer interactions within the aggregates of **P3HT-*b*-P3HTPMe₃**.²³ The PL and absorption data for both systems in D₂O and *d*₄-MeOD before and after the addition of surfactant are summarised in Table 1.

Table 1. Absorption (λ_{abs}) and PL (λ_{em}) maxima of the polythiophenes in D₂O and *d*₄-MeOD, before and after the addition of SDS and PFOS (1:1 charge ratio). $\lambda_{ex} = 450$ nm.

	Solvent	λ_{abs} (nm)	λ_{em} (nm)
P3HTPMe₃	D ₂ O	446	620
	<i>d</i> ₄ -MeOD	445	592
1:1 SDS	D ₂ O	598	679
	<i>d</i> ₄ -MeOD	446	582
1:1 PFOS	D ₂ O	447	620
	<i>d</i> ₄ -MeOD	417	572
P3HT-<i>b</i>-P3HTPMe₃	D ₂ O	535	732
	<i>d</i> ₄ -MeOD	518	630
1:1 SDS	D ₂ O	552	673
	<i>d</i> ₄ -MeOD	516	636
1:1 PFOS	D ₂ O	523	657
	<i>d</i> ₄ -MeOD	518	621

Effect of solvent. Solvent polarity has previously been shown to modulate the optical properties of the pure polythiophenes;²⁹ thus a similar effect was anticipated for the CPE-surfactant complexes. The normalised UV/Vis absorption spectra of **P3HTPMe₃** and **P3HT-*b*-P3HTPMe₃** with 1:1 charge ratio of SDS and PFOS in *d*₄-MeOD (10 mg mL⁻¹) are shown in Fig. 4a. Similar to D₂O, the absorption maximum of **P3HT-*b*-P3HTPMe₃** is significantly red-shifted (~70 nm) compared to **P3HTPMe₃**, and exhibits moderate vibronic structure. The addition of SDS results in a moderate blue-shift in λ_{abs} (~10 nm) and a narrowing of the absorption band for the homo- and diblock polymers. However, this shift is much smaller than observed for **P3HTPMe₃(SDS)₁** in D₂O (~150 nm), which indicates a smaller structural rearrangement in *d*₄-MeOD. More striking distinctions are observed upon the addition of PFOS. The absorption spectrum of **P3HTPMe₃(PFOS)₁** shows a blue-shift of ~30 nm, while the band for **P3HT-*b*-P3HTPMe₃(PFOS)₁** is significantly broader, which implies that the CPE adopts a more planar organisation.

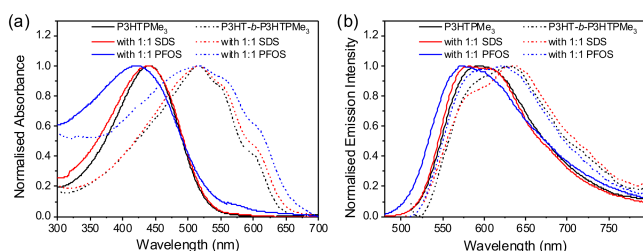


Figure 4. Effect of solvent on the optical properties of CPE-SDS_x complexes. Normalised (a) UV/Vis absorption and (b) emission spectra of **P3HTPMe₃** (solid black lines) and

P3HT-*b*-P3HTPMe₃ (dashed black lines) and the corresponding 1:1 SDS (red lines) and PFOS (blue lines) electrostatic complexes in *d*₄-MeOD (10 mg mL⁻¹).

P3HTPMe₃ and **P3HT-*b*-P3HTPMe₃** in *d*₄-MeOD also display distinctive PL spectra (Fig. 4b). **P3HTPMe₃** exhibits a broad, featureless emission band centred at 592 nm, while the emission spectrum of **P3HT-*b*-P3HTPMe₃** is broader still (520–850 nm) with well-resolved vibronic structure. The addition of SDS results in the emergence of vibronic structure for **P3HTPMe₃(SDS)₁** and **P3HT-*b*-P3HTPMe₃(SDS)₁**, while the addition of PFOS results in a blue-shift in the emission maximum to 572 and 621 nm for **P3HTPMe₃** and **P3HT-*b*-P3HTPMe₃**, respectively.

The dodecyl sulfate (DS⁻) and heptadecafluorooctane-sulfonate (PFOS⁻) counterions in complexes with **P3HTPMe₃** and **P3HT-*b*-P3HTPMe₃** are likely to hinder polymer-polymer interchain interactions, thereby decreasing the nominal effective conjugation length for exciton migration.²⁵ Previously, the complexation of DS⁻ with the related homopolymers P3TMAHT^{21, 22} and poly[3-(6'-(*N*-methylimidazolium)hexyl)thiophene-2,5-diyl] bromide (P3ImiHT)²³ was shown to induce significant surfactochromic transitions in aqueous solution, which could also be controlled by varying the surfactant charge ratio. However, the effect of SDS appears to be greater in D₂O than *d*₄-MeOD. There are two potential reasons for this: (1) these transitions are controlled to a large extent by the phase diagram of SDS. Micellization is known to be strongly inhibited by organic solvents, such as MeOH.⁵⁸ Therefore, while the critical micelle concentration (cmc) of SDS is well-known in water (cmc = ~8.2 mM)⁵⁹, there are few reliable records of the cmc in MeOH;⁶⁰ (2) the CPEs will also experience different phase transitions in methanol and water. Interestingly, PFOS has considerably more effect on the emission properties of **P3HTPMe₃** in *d*₄-MeOD than in D₂O. As with SDS, this is likely to be at least partially due to the difference in the cmcs of PFOS in MeOH and H₂O (~2 mM)⁶¹. Furthermore, this effect is significantly greater for the diblock copolymer vs. the homopolymer. The reduced charge density of the sulfonate head-group may enable PFOS to more effectively penetrate the neutral P3HT block core of the aggregates of **P3HT-*b*-P3HTPMe₃** than SDS. Fluorinated species, such as PFOS, may be expected to have an immiscibility gap with hydrogenated species, such as the CPES studied here, due to weaker van der Waals interactions.⁶² However, this may be counteracted by the high electronegativity of the fluorine atoms which will promote intermolecular interactions with P3HT through the formation of non-covalent F-S and F-H bonds.^{63, 64} In contrast, due to its higher charge density and hydrogenated tail, SDS can form stronger ionic and van der Waals associations with the **P3HTPMe₃** blocks, thus, explaining why greater surfactochromic changes are observed for the **P3HTPMe₃(SDS)_x** system.

Solution-phase structures

To obtain deeper insight into the nanoscale organisation of the polymers in solution, SANS studies were performed on the

P3HTPMe₃-surfactant and **P3HT-*b*-P3HTPMe₃**-surfactant complexes in D₂O and *d*₄-MeOD. Here, differences in the scattering length densities (SLDs) of individual components in the CPE-surfactant systems allow different zones of the complex to be probed. The SLDs of the surfactants differ significantly: SDS is closer to polythiophene, while *d*₂₅-SDS and PFOS are closer to D₂O and *d*₄-MeOD (Fig. 5). Therefore, CPE-SDS_{*x*} complexes will appear to neutrons as single entities, enabling the entire polymer-surfactant complex to be observed. In contrast, scattering from CPE-*d*₂₅-SDS and CPE-PFOS systems originates primarily from the polymer, allowing the organisation of the polymer *within* the complex to be investigated.

The observation window of these SANS experiments ranged from 2.6–70 nm, which covers the isolated chain lengths of the CPEs (22.2–30.4 nm) calculated from the length of the thiophene monomer (~0.4 nm).⁶⁵ The ratio of neutral:charged blocks is 59:4,1 which results in block lengths of 17.9 nm and 12.5 nm, respectively.⁶⁶ If the CPEs were dissolved down to the single molecule level, the SANS data would level off as a Guinier plateau at an experimentally obtainable *q* which is not observed here for any of the CPEs in D₂O or *d*₄-MeOD. All fits to the scattering profiles are summarised in Tables S3–S10 in the ESI†. Although it was not possible to obtain unique fits to the SANS data, all the chosen fits have absolute SANS intensities consistent with the known sample concentrations (~1% vol. dry material).

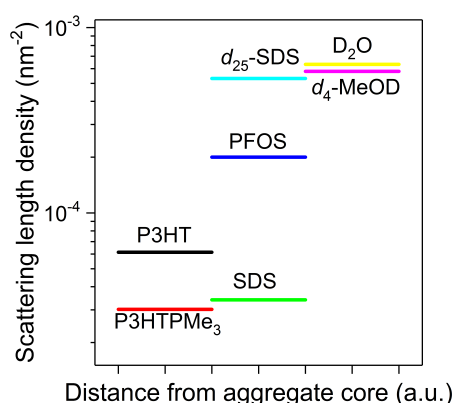


Figure 5. Comparison of the estimated neutron scattering length densities (SLDs) for the polymer blocks, surfactants and solvents used in the SANS studies. Materials with similar SLDs are considered *contrast matched*.

Homopolymer with surfactants in D₂O.

The related homopolymers P3TMAHT^{21, 22} and P3ImiHT²³ have previously been assigned as spherical aggregates in D₂O. However, a modest upturn at $q < 0.2 \text{ nm}^{-1}$ of $\sim q^{-1}$ implies that **P3HTPMe₃** may form cylindrical rather than spherical aggregates (Fig. 6a). Fitting of the SANS data ($0.08 < q < 2.2 \text{ nm}^{-1}$) to the Cylinder model^{46, 47} gave an aggregate length of 8.7 nm and radius of 1.5 nm. The hump at $q = 0.3 \text{ nm}^{-1}$ was accounted for by including a Hayter-Penfold structure factor, which accounts for particle-particle repulsive interactions.^{67–69} Alternatively, using a Guinier plot⁴⁶ (Fig. S4, ESI†) the

calculated radius of gyration (R_g) of aggregates of **P3HTPMe₃** in D₂O is 2.1 nm.

The scattering profile of **P3HTPMe₃** upon initial addition of hydrogenated SDS ($x = 0.2$) is quite different to that of the pure polymer (Fig. 6a), with an upturn at low q of $\sim q^{-1.7}$. This means that only a small amount of SDS (well below its cmc) is required to weaken the interparticle electrostatic ordering within aggregates of **P3HTPMe₃**.²³ Fitting of the SANS data ($0.08 < q < 2.2 \text{ nm}^{-1}$) to the Cylinder model^{46, 47} gave an aggregate length of 48.3 nm and radius of 1.8 nm. As the charge ratio is increased further from $x = 0.5$ to $x = 2$, there is a significant increase in scattering at low q ($q < 0.2 \text{ nm}^{-1}$). By $x = 1$, the scattering curve decays as $q^{-2.6}$, which is interpreted as the existence of “sheet-like” particles or larger smooth fractal aggregates, such as large or flocculated vesicles or a mixture of both.⁷⁰ The power law scaling at high q ($q > 1.0 \text{ nm}^{-1}$) starts to decay as q^{-4} , thus, marking the thickness of the sheet-like aggregates.²³ The upturn at $q = 0.8 \text{ nm}^{-1}$, could be repulsion between similarly charged chains or the appearance of free SDS micelles, considering that the concentration is well above the cmc of SDS in water ($8.2 \text{ mM} \approx 2.4 \text{ mg mL}^{-1}$).⁷¹ Fitting with the Lamellar Sheet model^{48, 49} gave sheet thicknesses (T_{sheet}) of 1.0, 2.0 and 1.4 nm for $x = 0.5$, 1 and 2, respectively. These thicknesses correspond to the solid state *d*-spacing of poly(3-hexylthiophene) (~1.7 nm)⁶⁵ or the length of individual SDS molecules (~2.5 nm),⁷² implying that the polymer and surfactant must be interwoven rather than forming well-defined layers.²³ At $x = 5$, the scattering intensity scales as $q^{-0.5}$, and the data can be fitted as spherical aggregates with a radius of 2.5 nm and 65% solvent content (Fig. S7, ESI†). This is only slightly larger than pure SDS micelles, which are also spherical with radius of ~1.9 nm (Fig. 6a, red circles). This suggests that scattering from the $x = 5$ sample occurs predominantly from SDS micelles, with the **P3HTPMe₃** associating to their surfaces, which may potentially explain the slight increase in radius.

Fig. 6d shows the SANS data and fits for **P3HTPMe₃(*d*₂₅-SDS)_{*x*}** in D₂O, in which the scattering profile mainly arises from **P3HTPMe₃** within the **P3HTPMe₃(*d*₂₅-SDS)_{*x*}** associations. After addition of *d*₂₅-SDS up to $x = 1$, the SANS data exhibit a strong upturn at low q , described empirically by a power law scaling of $q^{-2.7}$, strongly resembling that of **P3HTPMe₃(SDS)₁** (Fig. 6e). The data indicate that **P3HTPMe₃** forms sheet-like aggregates *within* the sheet-like CPE-SDS_{*x*} associations and can be fitted to the Lamellar Sheet model^{48, 49} to give a T_{sheet} of 3.4 nm for $x = 1$, surprisingly thicker than for **P3HTPMe₃(SDS)₁** (~2.0 nm). Interestingly, the scattering profile for **P3HTPMe₃(*d*₂₅-SDS)₅** is clearly still reminiscent of lamellar sheets ($\sim q^{-2}$). In contrast, the apparent spherical scattering profile in **P3HTPMe₃(SDS)₅** is likely to be a consequence of the micelles formed from the excess SDS.

The analogous SANS profiles for **P3HTPMe₃(PFOS)_{*x*}** can be found in Fig. S7 (ESI†). For $x = 1$, the data show a strong upturn at low q , described by $q^{-2.3}$ scaling, strongly resembling that of **P3HTPMe₃(SDS)₁** (Fig. 6c). This implies the complexes also form sheet-like aggregates; however, fitting with the Lamellar Sheet model gave considerably thicker sheets ($T_{\text{sheet}} = 4.8 \text{ nm}$).^{48, 49} The increase is likely to be due to the increased

rigidity of the surfactant tail and reduced charge density of the sulfonate head-group, making PFOS less able to penetrate the existing **P3HTPMe₃** aggregates compared to SDS or *d*₂₅-SDS,²¹ and resulting in more distinct “**P3HTPMe₃**” and “PFOS” layers.

Diblock copolymer with surfactants in D₂O. The SANS data of **P3HT-*b*-P3HTPMe₃** in D₂O (Fig. 6b) yield a similar scattering profile to the pyridinium (Py) and imidazolium (Im) **P3HT-*b*-P3HTX** analogues previously studied,²⁹ with a shoulder at $q = 0.2 \text{ nm}^{-1}$ and an upturn at $q = 0.8 \text{ nm}^{-1}$. The low q region ($q < 0.2 \text{ nm}^{-1}$) decays as $q^{-1.6}$, which is typical of scattering from either cylindrical aggregates or individual chains.⁷³ At high q ($q > 0.7 \text{ nm}^{-1}$), the SANS response stems from the internal

structure of the aggregate. The data ($0.08 < q < 2.0 \text{ nm}^{-1}$) were thus fit to a Core-Shell Cylinder model,⁵⁰ which indicates that **P3HT-*b*-P3HTPMe₃** forms aggregates with a dry core (~5% solvent), a radius (r_{core}) of 47.2 Å, length (L_{core}) of 51.8 nm, and a thick, wet shell (~82% solvent) of 7.0 nm. The SLDs of the P3HT and P3HTPMe₃ blocks are both $\sim 1 \times 10^{-4} \text{ nm}^{-2}$ (Fig. 5). Therefore, they can only be distinguished by neutron scattering when one block is substantially more solvated than the other. Here, core-shell cylinders with hydrophobic, neutral block cores and solvated, hydrophilic charged block shells are observed.

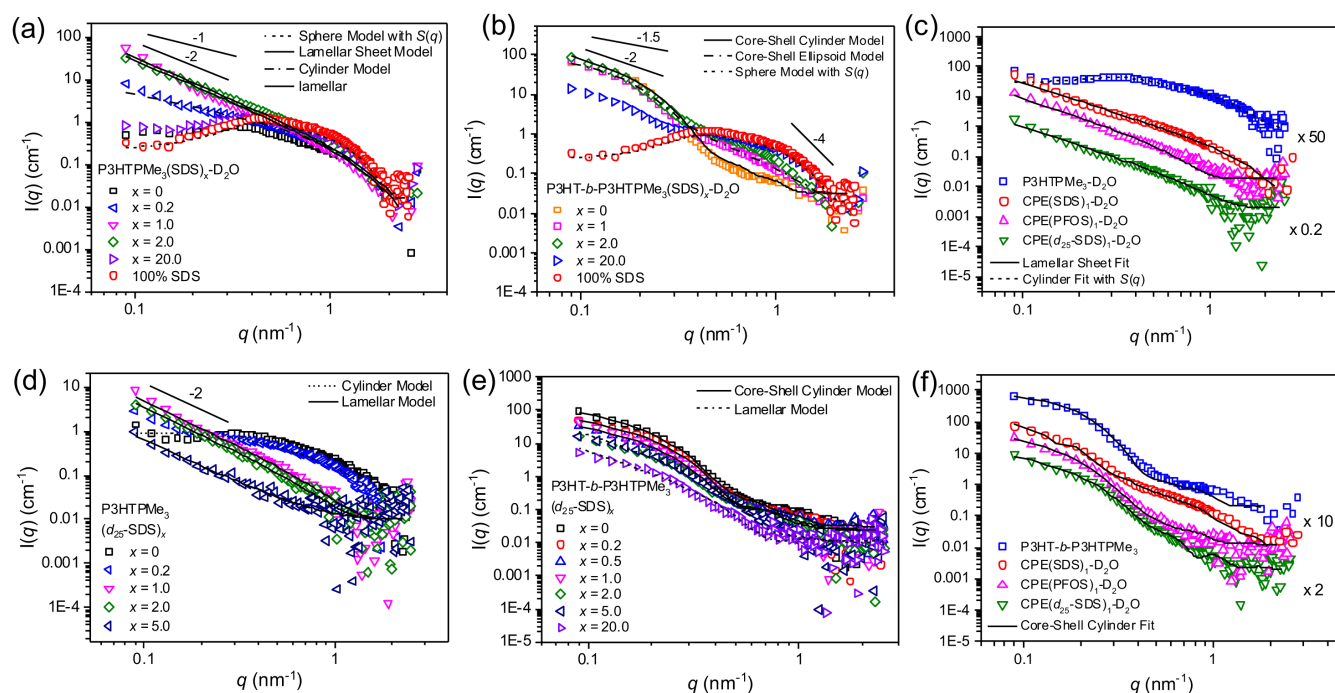


Figure 6. Effect of surfactant type and charge ratio, x , on the solution phase structures of **P3HTPMe₃** and **P3HT-*b*-P3HTPMe₃**. SANS data of **P3HTPMe₃** and **P3HT-*b*-P3HTPMe₃** in D₂O with selected charge ratios of (a,b) SDS and (d,e) *d*₂₅-SDS, respectively. Straight lines show q^{-1} , $q^{-1.5}$, q^{-2} and q^{-4} for comparison. (c) **P3HTPMe₃** and (f) **P3HT-*b*-P3HTPMe₃** (blue squares) in D₂O and with 1:1 charge ratio of SDS (red circles), PFOS (pink triangle) and *d*₂₅-SDS (green triangles). Solid, dashed and dot-dashed lines represent the fits described in the text. The overall concentration of each system was 10 mg mL⁻¹. $T = 25 \text{ }^\circ\text{C}$. Error bars were omitted to enable the slopes to be better distinguished. Representative error bars can be seen in the ESI†.

Initially, there is practically no change in the scattering profile of **P3HT-*b*-P3HTPMe₃** upon addition of hydrogenated SDS ($x = 0.2$) (Fig. 6d). However, by increasing the charge ratio ($x = 0.5$), an increase in the scattering intensity is observed at $q = 0.8 \text{ nm}^{-1}$, indicative of repulsion between similarly charged chains. In addition, by $x = 1$ the shoulder at $q = 0.2 \text{ nm}^{-1}$ becomes less pronounced and the profile scales as q^{-2} . This implies that the core-shell cylinders of the pure diblock copolymer transform into 2D sheets upon coordination with SDS. At $x = 2$ and $x = 5$ the q -scaling decreases to $q^{-1.9}$ and $q^{-1.7}$, respectively, indicating the progressive loss of the lamellar sheet structure upon increasing charge ratio. The SANS data ($0.08 < q < 2.0 \text{ nm}^{-1}$) of **P3HT-*b*-P3HTPMe₃(SDS)_x** were fit to the Core-Shell Cylinder,⁵⁰ Lamellar Sheet^{48, 49} or Sphere models, shown in Fig. 6b and summarised in the Table S5, ESI†. The fits for the **P3HT-*b*-P3HTPMe₃(SDS)_x** system proved particularly difficult to

optimise. For $x = 0.2$ and $x = 0.5$, the samples were fit using the Core-Shell Cylinder model. Although the core lengths and radii are similar to those of the parent diblock copolymer, the shell appears to become thicker and drier. However, it must be noted that these fits were not perfect, and are particularly poor at $q = 0.8 \text{ nm}^{-1}$. At $x = 1$, the charge compensation point, the scattering profile was best fit to the Lamellar Sheet model,^{48, 49} with a T_{sheet} of 5.9 nm. Although this fit was again not ideal, it was significantly better than the alternative fit using the Core-Shell Cylinder model.⁵⁰ For $x = 5$ and $x = 20$, fits of satisfactory quality to the entire data were not possible. However, the high q data ($0.27 < q < 2.4 \text{ nm}^{-1}$) strongly resembled the scattering from pure SDS micelles, and a fit to the Spherical model⁴⁶ resulted in radii of 2.7 and 2.3 nm for $x = 5$ and $x = 20$, respectively. This implies that by $x = 5$, **P3HT-*b*-P3HTPMe₃(SDS)_x** exists mainly as SDS micelles, potentially with

associating CPE chains on the surface to account for the slight increase in radius compared to pure SDS micelles.

Interestingly, when contrast-matching with the deuterated surfactant analogue (d_{25} -SDS) is performed, the scattering profiles of the entire **P3HT-*b*-P3HTPMe₃(d_{25} -SDS)_{*x*}** series strongly resemble the core-shell cylinder profile of the parent diblock copolymer (Fig. 6e). The Core-Shell Cylinder model was fit to each of the scattering profiles and the fitting parameters are summarised in the Table S6 in the ESI†. At $x = 1$, the fit gave an elongated cylinder with L_{core} of 47.7 nm, r_{core} of 4.9 nm and T_{shell} of 7.1 nm. Each of the fits was greatly improved by adding polydispersity to the core radius. Therefore, we propose that since lamellar sheets are observed with SDS, and yet core-shell cylinders dominate when the surfactant has been contrast-matched, the SDS may act to connect adjacent **P3HT-*b*-P3HTPMe₃** cylinders to form two-dimensional, sheet-like arrays.

Fitting with the Core-Shell Cylinder model to the **P3HT-*b*-P3HTPMe₃(PFOS)_{*x*}** series also gave core-shell cylinders with hydrophobic, neutral block cores and solvated, hydrophilic charged block shells (Fig. S4b, ESI†). The SLD of PFOS ($2 \times 10^{-4} \text{ nm}^{-2}$) is quite well contrast-matched with D₂O, and as a result the scattering is expected to mainly occur from the polymer. At $x = 1$, shown in Fig. 6f, the fit gave a wide, (relatively) wet core with r_{core} of 5.9 nm (16% wetness), a shorter L_{core} of 46.6 nm, and thick, wet T_{shell} of 7.8 nm (85% wetness) (Fig. 8c). Notably, PFOS, unlike SDS, induced a significant increase in the “wetness” of the neutral P3HT cores.

Effect of solvent. The SANS data for **P3HTPMe₃** and **P3HT-*b*-P3HTPMe₃** at 1:1 charge ratio with SDS in d_4 -MeOD have been discussed in depth in previous work,²⁹ and thus will only be briefly recapped here for the sake of comparison with the analogous samples in D₂O. **P3HTPMe₃** in d_4 -MeOD adopts a flexible rod-like conformation with a high solvent content (>85% solvent) and total cylinder length (90.0 nm), and a radius of 1.3 nm, while in D₂O it forms charged spherical aggregates ($R_g \sim 2.1 \text{ nm}$) with interparticle interactions. **P3HTPMe₃** in d_4 -MeOD better resembles the scattering profiles obtained when this CPE or the analogous homopolymers, P3TMAHT and P3ImiHT,^{21, 22} are combined with a small amount of SDS (CPE/surfactant charge ratio of 1:0.2) in D₂O. In all three systems, the pure CPE aggregates are believed to disassemble and reorganise into CPE-surfactant cylinders.^{21, 22} This suggests that **P3HTPMe₃** forms more ordered aggregates in d_4 -MeOD, with significant packing between CPE chains. **P3HTPMe₃(SDS)₁** in d_4 -MeOD favours a lamellar-type structure ($T_{\text{sheet}} \sim 4.7 \text{ nm}$, $\sim 50\%$ solvent) believed to be comprised of distinct **P3HTPMe₃** and SDS layers, rather than the interwoven sheets expected in D₂O.

In contrast, both **P3HT-*b*-P3HTPMe₃** and **P3HT-*b*-P3HTPMe₃(SDS)₁** in d_4 -MeOD form core-shell cylindrical aggregates in solution, with the P3HT block comprising the core and the P3HTPMe₃ block (and associated counterions) forming the shell. Thus, unlike in D₂O, counterion exchange yields only subtle changes in the scattering profile for **P3HT-*b*-P3HTPMe₃(SDS)₁- d_4 -MeOD**, without the apparent formation of

lamellar sheets. These results indicate that solution structure of **P3HT-*b*-P3HTPMe₃** in d_4 -MeOD and D₂O is primarily dictated by the hydrophobic P3HT core, which “locks-in” the cylindrical morphology of the pure diblock polymer upon surfactant addition. In comparison, the less-restricted **P3HTPMe₃** is able to freely transform from semi-flexible cylinders to rigid sheets upon counterion exchange in both solvents.

Cryo-transmission electron microscopy.

It is important to note that when the diameter of a vesicle is well outside the q -window of a SANS experiment (3.0 to 69.8 nm here), then the scattering would appear to correspond to that of lamellar sheets (q^{-2}). In order to investigate whether this was the case here, direct imaging by cryo-TEM has been utilised to visualise the particle size and morphology in D₂O. This technique has the advantage that the micelles can be observed in their hydrated state and that the aqueous environment remains undisturbed.

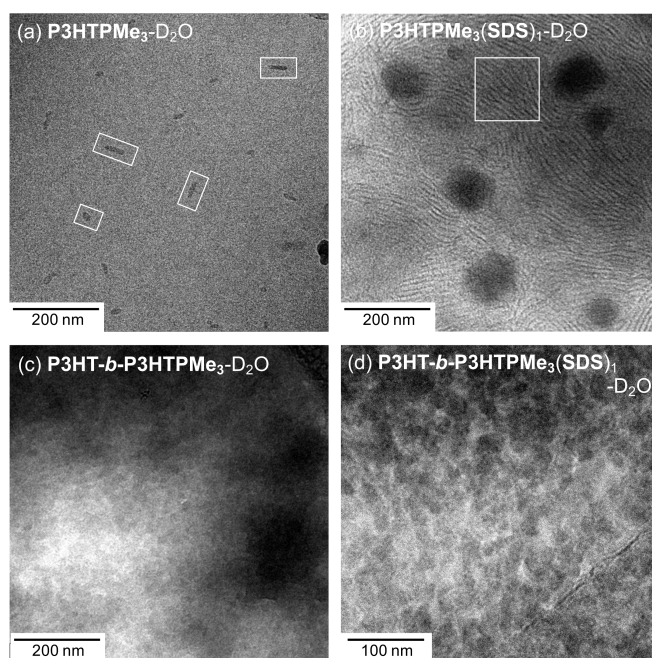


Figure 7. Cryo-TEM micrographs of (a) **P3HTPMe₃**, (b) **P3HTPMe₃(SDS)₁**, (c) **P3HT-*b*-P3HTPMe₃** and (d) **P3HT-*b*-P3HTPMe₃(SDS)₁**. Total concentration = 10 mg mL⁻¹.

Cylindrical or rod-like particles were observed for **P3HTPMe₃**-D₂O, as shown in Fig. 7a, with average width of 7.5 (± 2.3) nm and length of 30.6 (± 14.0) nm. Such rod-like structures have previously been observed for P3HT in vitrified organic solvents such as toluene and 1,2-dichlorobenzene,⁷⁴ and were attributed to π - π packing of the conjugated polythiophene backbones. Upon the addition of SDS a remarkable change in morphology is observed with the formation of two notable features: (1) large spherical aggregates, ~ 73.9 (± 15.3) nm in diameter, which could be vesicles, although vesicles are more typically capsule-like. More likely, these regular features are simply aggregates of CPE and/or SDS that form reasonably homogeneous nanoparticles (Fig. S8, ESI†); (2) lamellar-type striations, highlighted by the white box in Fig. 7b, with sheet thicknesses of 4.0 (± 1.1) nm, which agree well the

observations made by SANS. Similar thread-like micelles were previously observed in cryo-TEM images of mixtures of SDS and the organic salt 1,2-bis(2-benzylammoniummethoxy dichloride) (BEO) in a 5:1 ratio in H₂O when the concentration is high ([SDS] = 15 mM).⁷⁵

Given the difficulty in fitting unique structures to the SANS data, it is therefore not surprising that distinctive features

were harder to identify in for **P3HT-*b*-P3HTPMe₃** samples. However, spherical structures, 19.8 (±3.6) nm in diameter, can definitely be identified in Fig. 7c, which are approximately the same sizes as determined from the model fitting of SANS data. The spheres become much more distinctive upon addition of SDS, with slightly larger diameters of 21.7 (±3.5) nm.

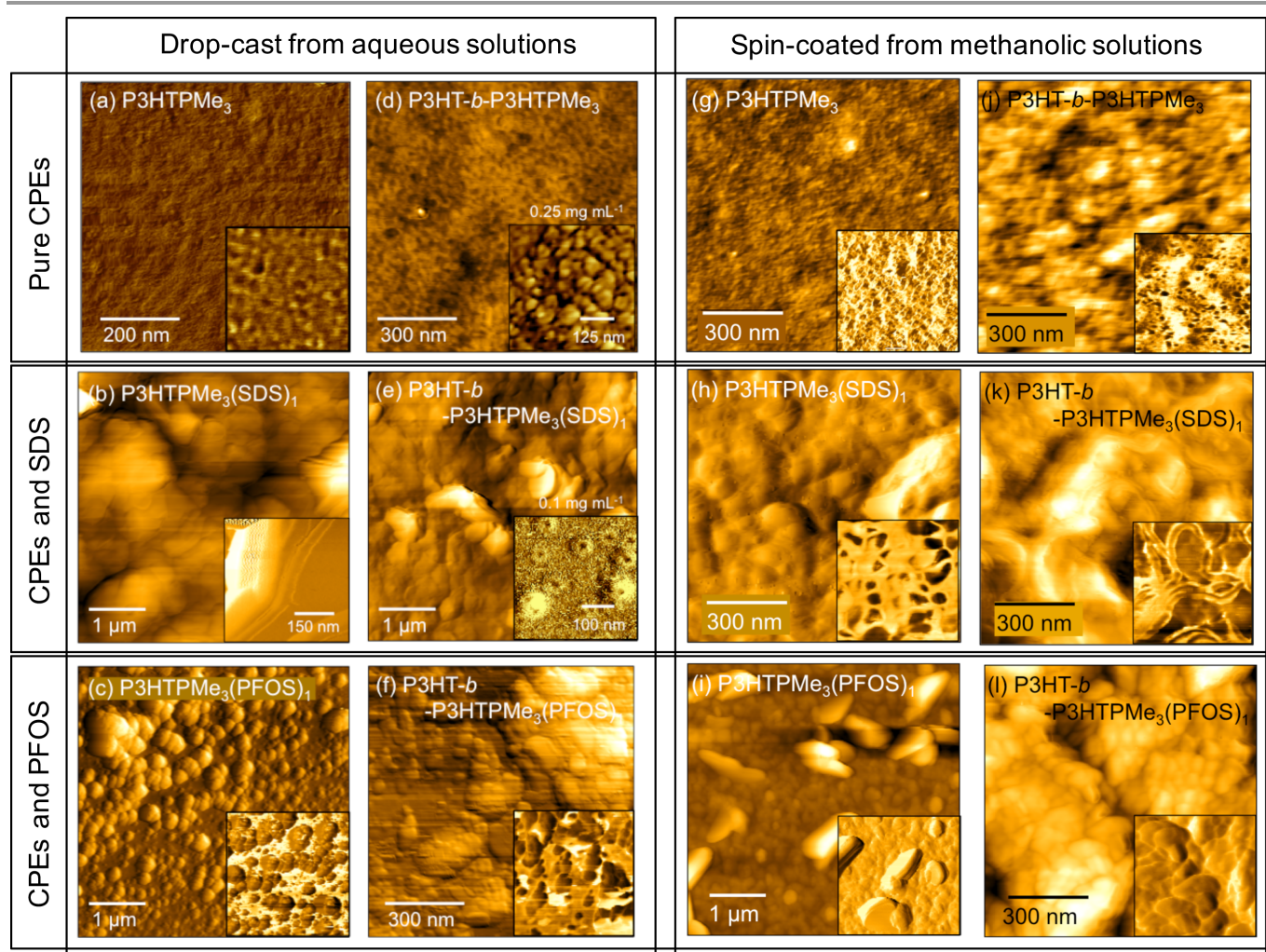


Figure 8. AFM tapping-mode height images of pure CPEs and CPE-surfactant complexes at 1:1 charge ratio prepared in water (a-f) and methanol (g-l) (10 mg mL⁻¹). AFM images of (a) P3HTPMe₃ and (d) P3HT-*b*-P3HTPMe₃ with (b,e) SDS and (c,f) PFOS, respectively, drop-cast from H₂O. AFM images of (g) P3HTPMe₃ and (j) P3HT-*b*-P3HTPMe₃ with (h,k) SDS and (i,l) PFOS, respectively, spin-coated from MeOH. Insets: phase images at the same concentration and magnification unless otherwise stated.

Thin film morphology

AFM was used to investigate the correlation between the nanoscale organisation of aggregates formed in solution and the morphology of subsequently cast thin films. Thin films of pure CPEs and CPE-surfactant complexes dissolved in MeOH were spin-coated onto silicon substrates. Unfortunately, it was not possible to obtain spin-coated films of samples dissolved in H₂O due to the hydrophobicity of the silicon substrates.⁷⁶ Therefore, all the films of the H₂O samples were prepared *via* drop-casting.

The surface morphology was found to be dependent on the type of polythiophene (homo- vs. diblock copolymer), solvent

and presence and nature of surfactant. In water, P3HTPMe₃ formed mainly featureless films (Fig. 8a), which is not surprising since it is expected to be well-dissolved with minimal assembly into spheres or rods. In contrast, films of P3HTPMe₃(SDS)₁ consisted of large aggregates with smooth flat surfaces. The inset phase image in Fig. 8b shows more clearly the formation of sheet-like domains, with a spacing of ~50 nm. P3HTPMe₃(PFOS)₁ forms a collection of polydisperse spheres (Fig. 8c) that show no resemblance to the parent homopolymer or P3HTPMe₃(SDS)₁.

P3HT-*b*-P3HTPMe₃ forms large clusters of small, polydisperse spheres, with an average diameter of 36.0 ± 7.7

nm (Fig. 8d). For **P3HT-*b*-P3HTPMe₃(SDS)₁** (10 mg mL⁻¹), it was difficult to distinguish any clear features within the extremely amorphous surface morphology (Fig. 8e). However, upon dilution (×100), we can clearly see spheres, whose core-shell structure is visible in the phase image (Fig. 8e inset). The average diameter was 55.0 ± 10.4 nm, with an average core diameter of 17.6 ± 3.9 nm. **P3HT-*b*-P3HTPMe₃(PFOS)₁** forms a significantly less distinct surface, with some small spheres (~30 nm) appearing at the edge of larger, amorphous aggregates.

Given that the concentrations of SDS and PFOS in the aqueous samples are greater than the cmcs of the pure surfactants,^{61, 71} it is reasonable to expect the coexistence of surfactant micelles only if there is incomplete association between the CPE and surfactant. However, most of CPE-SDS_x complexes formed films with distinctive morphologies when compared to the films of the pure surfactant (Fig. S9, ESI†). The only exception was **P3HTPMe₃(PFOS)₁** which formed a collection of polydisperse spheres which resembled pure PFOS.

In MeOH, **P3HTPMe₃** also forms largely featureless films (Fig. 8g), with small spherical aggregates (10-20 nm) only apparent in the phase image. Complexation with SDS produces large globules (~100 nm), which appear from the phase image to be potentially vesicles (Fig. 8h). In contrast, complexes formed with PFOS formed a generally flat plane of spheres, dispersed with significantly larger, flat structures (Fig. 8i). The high-resolution image shown in the inset clearly shows the lamellar structure within these aggregates.

P3HT-*b*-P3HTPMe₃ in MeOH formed quite uniform films of spheres (~30 nm in diameter), which appear to have core-shell structure in the phase image. Complexation with SDS (Fig. 8k) shows some spherical aggregates without any distinctive boundaries. There appears to be a continuous network running through this image, implying that CPE aggregates are more interdispersed with SDS. In contrast, **P3HT-*b*-P3HTPMe₃** with PFOS, which is expected to interact less effectively with the P3HTPMe₃, appears to retain the spherical structure from imparted by the parent copolymer more effectively. The observed spheres of **P3HT-*b*-P3HTPMe₃-PFOS** complexes are significantly larger (~60 nm), which supports the larger core radius indicated by SANS. Blank films of pure SDS and PFOS prepared from MeOH bore no resemblance to any of the CPE-surfactant films (Fig. S10, ESI†).

Proposed self-assembly structures

Figure 9 shows a schematic representation of the proposed aggregate structures adopted by **P3HTPMe₃** and **P3HT-*b*-P3HTPMe₃** upon surfactant complexation and in different solvents. The SANS fits and cryo-TEM data for **P3HTPMe₃** in D₂O suggest it forms either short-cylinders or spherical aggregates (Fig. 9a). Upon addition of SDS, a significant colour change is observed, from the red-aggregated phase to a yellow solution of disrupted aggregates. The emergence of vibronic structure in the PL spectra for $x = 0.2 - 2$, implies the formation of rigid, compact planar aggregates. This observation agrees well with the SANS and cryo-TEM studies, which suggest the formation of sheets comprised of intimate blends of CPE and surfactant. High charge ratios led to the

formation of isolated SDS micelles, although it was evident from contrast-matching SANS experiments that **P3HTPMe₃-SDS** sheet complexes persist until $x = 5$.

In contrast, SDS has only a limited effect on the solution structure of **P3HT-*b*-P3HTPMe₃**, with the hydrophobic P3HT core retaining the cylindrical morphology of the pure diblock copolymer (Fig. 9b). As D₂O is a selective solvent for the charged CPE block, the core is expected to consist predominantly of the neutral P3HT blocks, which are surrounded by a highly solvated CPE shell. Optical and SANS studies indicated that polymer-polymer packing within the shell was affected by the presence and concentration of surfactant, which supports this assignment. With increasing SDS, an increase in the wetness and thickness of the CPE block shell was observed, which corresponds to a reorganisation of P3HTPMe₃ chains. In contrast, the P3HT core was relatively unaffected, which may account for the retention of some vibronic structure in the PL spectra beyond $x = 1$. The SANS data suggest that the **P3HT-*b*-P3HTPMe₃(SDS)₁** uniquely adopts a sheet-like structure and contrast-matching experiments with d_{25} -SDS make it possible to see how the macromolecular structure within such aggregates may form. As such, the core-shell cylinder aggregates of **P3HT-*b*-P3HTPMe₃-SDS** are proposed to bind together with the help of SDS to form lamellar sheets (Fig. 9b).

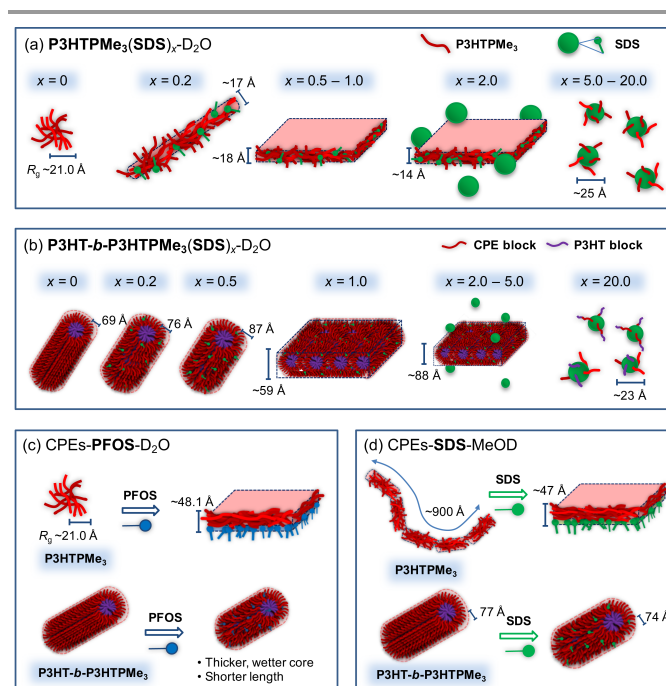


Figure 9. Schematic representation of the proposed self-assembly structures of (a) **P3HTPMe₃** and (b) **P3HT-*b*-P3HTPMe₃** with increasing charge ratios, x , of SDS in D₂O. Schematic representation of the proposed self-assembly structures of **P3HTPMe₃** and **P3HT-*b*-P3HTPMe₃** before and after the addition of (c) 1:1 charge ratio of PFOS in D₂O and (d) 1:1 charge ratio of SDS in d_4 -MeOD.

Striking differences are also observed between how the homo- and diblock CPEs interact with PFOS (Fig. 9c). Theoretical studies have shown that sulfate and sulfonate groups differ significantly in their charge density ($\delta_{CD} = -1.13$

and -0.66, respectively)⁵⁷. The reduced charge density of the sulfonate group in PFOS suggests that electrostatic interactions between **P3HTPMe₃** and PFOS will occur predominantly at the aggregate surface, where the interaction forms sheet-like aggregates, but does not alter the effective conjugation length of the **P3HTPMe₃** backbone; thus, the optical properties are essentially unchanged. This corresponds well to the sheet thickness obtained from the SANS fits which suggest that distinct PFOS/CPE layers are present. While **P3HT-*b*-P3HTPMe₃-PFOS_x** retains the core-shell cylinder structure, a striking increase in the wetness and radius of the P3HT core at $x = 1$ is observed compared to the pure CPE. Taking this into consideration with the optical observations, we propose that PFOS is able to penetrate the neutral P3HT core, causing some degree of structural rearrangement to the neutral polymer-polymer associations. The lower charge density of the sulfonate head group, coupled with the inductive effect of the fluorinated backbone, implies that weaker electrostatic interactions should be expected between the phosphonium group of the CPEs and PFOS than with SDS. Therefore, the more weakly-charged PFOS may also be expected to penetrate more deeply within the neutral P3HT blocks of the diblock copolymer than SDS.⁷⁷

Methanol is a better solvent for device fabrication than water due to its higher volatility. While the optical properties of **P3HTPMe₃** and **P3HT-*b*-P3HTPMe₃** in MeOD showed only a minor dependence on the nature of the counterion, the aggregate structures formed strongly resemble those in D₂O, although with subtle differences (Fig. 9d). **P3HTPMe₃** formed a flexible rod-like conformation with high solvent content, while **P3HTPMe₃(SDS)₁** favoured a lamellar-type structure believed to be comprised of distinct, rather than interwoven, **P3HTPMe₃** and SDS layers. In contrast, **P3HT-*b*-P3HTPMe₃** and **P3HT-*b*-P3HTPMe₃(SDS)₁** formed core-shell cylinder aggregates, with a P3HT core and a CPE-SDS shell.

Notably, the aggregate structures formed in solution could be effectively transferred to films deposited by both spin-coating and drop-casting. The addition of surfactants to solutions of **P3HTPMe₃** induced nanoscale phase separation in the resultant films, with the observation of lamellar-like regions. **P3HT-*b*-P3HTPMe₃** films formed core-shell spherical structures, somewhat in contrast to the core-shell cylinder or lamellar structures indicated by SANS. However, SANS also indicated that aggregates of **P3HT-*b*-P3HTPMe₃** possessed solvated, wet shells. It is therefore conceivable that the removal of the solvent during drying of the film may lead to partial reorganisation or shrinkage of the aggregate structure. The **P3HT-*b*-P3HTPMe₃**-surfactant films exhibited less distinct spherical or sometimes amorphous structures, suggesting complete or partial collapse of the core-shell structure. It is interesting to note that the majority of core-shell structures identified in solution are retained in the films spin-coated from methanol, since one potential drawback of spin-coating is that it is known to reduce the crystallinity of P3HT thin films by preventing appropriate alignment of the polymer chains.⁷⁸

Conclusions

While the optical properties of **P3HTPMe₃** and **P3HT-*b*-P3HTPMe₃** show a moderate dependence on the nature of the surfactant counterion, its concentration and the solvent, stark transitions in the solution structures are observed upon modifying these parameters. **P3HTPMe₃** has been shown to freely transform from spheres or semi-flexible cylinders to rigid sheets upon association with anionic surfactants, the size and morphology of which is dependent of the surfactant charge density, tail length and stiffness and solvent. In contrast, surfactants only have a limited effect on the solution structure of **P3HT-*b*-P3HTPMe₃**, with the hydrophobic P3HT core retaining the cylindrical morphology of the pure diblock copolymer. However, contrast-matching SANS experiments with deuterated surfactants have indicated how the macromolecular organisation between **P3HT-*b*-P3HTPMe₃**-SDS aggregates is formed. Furthermore, the reduced charge density of perfluorinated surfactants may offer an effective route to tune the polymer-polymer packing density within the P3HT-cores.

It is perhaps unsurprising that homopolymers vs. diblock copolymers yield significantly different self-assembled structures. However, the structure “lock-in” tendency of the hydrophobic P3HT block, coupled with subtle differences in the surfactant mole fraction, chemical structure and solvent polarity (MeOH vs. H₂O) give rise to remarkable variations in the range and type of complexes formed affecting both the solution phase structures and the morphology of the thin films. This has important consequences for future device preparation. For example, it has recently been shown that while charge generation occurs in the ordered domains of semi-crystalline P3HT films, the connectivity of these ordered domains through long polymer chains can strongly enhance charge transport.⁷⁹ Thus, the ability to control the chain packing within CPE aggregates could be harnessed to balance the charge carrier ability with other physical properties of films currently being considered for OPV devices.^{78, 80}

Acknowledgements

SC and MC thank the CNRS and the Université de Montpellier for financial support. Support from COST action MP1202 and the Ireland-France “Hubert Curien Ulysses” programme (grant no. 31998ZF) is gratefully acknowledged. We thank ISIS and STFC for the allocation of SANS beamtime (experiment RB 1510199). This work benefitted from SasView software, originally developed by the DANSE project under NSF award DMR-0520547.

Notes and references

1. H. Jiang, P. Taranekekar, J. R. Reynolds and K. S. Schanze, *Angew. Chem. Inter. Ed.*, 2009, **48**, 4300-4316.
2. Z. Ren, R. S. Nobuyasu, F. B. Dias, A. P. Monkman, S. Yan and M. R. Bryce, *Macromolecules*, 2016, **49**, 5452-5460.

3. X. Yang, G. Zhou and W.-Y. Wong, *J. Mater. Chem. C*, 2014, **2**, 1760-1778.
4. W. Lee, J. H. Seo and H. Y. Woo, *Polymer*, 2013, **54**, 5104-5121.
5. H. Siringhaus, *Adv. Mater.*, 2014, **26**, 1319-1335.
6. R. S. Ashraf, I. Meager, M. Nikolka, M. Kirkus, M. Planells, B. C. Schroeder, S. Holliday, M. Hurhangee, C. B. Nielsen, H. Siringhaus and I. McCulloch, *J. Am. Chem. Soc.*, 2015, **137**, 1314-1321.
7. C. B. Nielsen, A. Giovannitti, D.-T. Sbircea, E. Bandiello, M. R. Niazi, D. A. Hanifi, M. Sessolo, A. Amassian, G. G. Malliaras, J. Rivnay and I. McCulloch, *J. Am. Chem. Soc.*, 2016, **138**, 10252-10259.
8. J. Hwang, J. Park, Y. J. Kim, Y. H. Ha, C. E. Park, D. S. Chung, S.-K. Kwon and Y.-H. Kim, *Chem. Mater.*, 2017, **29**, 2135-2140.
9. S. Liu, P. You, J. Li, J. Li, C.-S. Lee, B. S. Ong, C. Surya and F. Yan, *Energy Environ. Sci.*, 2015, **8**, 1463-1470.
10. J. Yuan, C. McDowell, C.-K. Mai, G. C. Bazan and W. Ma, *Chem. Mater.*, 2016, **28**, 7479-7486.
11. Z. Hu, K. Zhang, F. Huang and Y. Cao, *Chem. Commun.*, 2015, **51**, 5572-5585.
12. J.-S. Yu, I. Kim, J.-S. Kim, J. Jo, T. T. Larsen-Olsen, R. R. Sondergaard, M. Hosel, D. Angmo, M. Jorgensen and F. C. Krebs, *Nanoscale*, 2012, **4**, 6032-6040.
13. M. Singh, H. M. Haverinen, P. Dhagat and G. E. Jabbour, *Adv. Mater.*, 2010, **22**, 673-685.
14. H. Zheng, Y. Zheng, N. Liu, N. Ai, Q. Wang, S. Wu, J. Zhou, D. Hu, S. Yu, S. Han, W. Xu, C. Luo, Y. Meng, Z. Jiang, Y. Chen, D. Li, F. Huang, J. Wang, J. Peng and Y. Cao, *Nat. Commun.*, 2013, **4**, 1971.
15. L. Ying, F. Huang and G. C. Bazan, *Nat. Commun.*, 2017, **8**, 14047.
16. R. C. Evans, *J. Mater. Chem. C*, 2013, **1**, 4190-4200.
17. H. D. Burrows, S. M. Fonseca, C. L. Silva, A. A. C. C. Pais, M. J. Tapia, S. Pradhan and U. Scherf, *Phys. Chem. Chem. Phys.*, 2008, **10**, 4420-4428.
18. C. Tan, M. R. Pinto and K. S. Schanze, *Chem. Commun.*, 2002, 446-447.
19. H. D. Burrows, M. J. Tapia, C. L. Silva, A. A. C. C. Pais, S. M. Fonseca, J. Pina, J. Seixas de Melo, Y. Wang, E. F. Marques, M. Knaapila, A. P. Monkman, V. M. Garamus, S. Pradhan and U. Scherf, *J. Phys. Chem. B*, 2007, **111**, 4401-4410.
20. L. Chen, S. Xu, D. McBranch and D. Whitten, *J. Am. Chem. Soc.*, 2000, **122**, 9302-9303.
21. R. C. Evans, M. Knaapila, N. Willis-Fox, M. Kraft, A. Terry, H. D. Burrows and U. Scherf, *Langmuir*, 2012, **28**, 12348-12356.
22. M. Knaapila, R. C. Evans, V. M. Garamus, L. s. Almásy, N. m. K. Székely, A. Gutacker, U. Scherf and H. D. Burrows, *Langmuir*, 2010, **26**, 15634-15643.
23. M. Knaapila, R. C. Evans, A. Gutacker, V. M. Garamus, N. K. Szekely, U. Scherf and H. D. Burrows, *Soft Matter*, 2011, **7**, 6863-6872.
24. J. J. Lavigne, D. L. Broughton, J. N. Wilson, B. Erdogan and U. H. F. Bunz, *Macromolecules*, 2003, **36**, 7409-7412.
25. H. D. Burrows, V. M. M. Lobo, J. Pina, M. L. Ramos, M. J. S. de, A. J. M. Valente, M. J. Tapia, S. Pradhan and U. Scherf, *Macromolecules*, 2004, **37**, 7425-7427.
26. M. Knaapila, L. Almásy, V. M. Garamus, C. Pearson, S. Pradhan, M. C. Petty, U. Scherf, H. D. Burrows and A. P. Monkman, *The J. Phys. Chem. B*, 2006, **110**, 10248-10257.
27. M. J. Robb, S.-Y. Ku and C. J. Hawker, *Adv. Mater.*, 2013, **25**, 5686-5700.
28. R. Verdusco, I. Botiz, D. L. Pickel, S. M. Kilbey, K. Hong, E. Dimasi and S. B. Darling, *Macromolecules*, 2011, **44**, 530-539.
29. A. Thomas, J. E. Houston, N. Van den Brande, J. De Winter, M. Chevrier, R. K. Heenan, A. E. Terry, S. Richeter, A. Mehdi, B. Van Mele, P. Dubois, R. Lazzaroni, P. Gerbaux, R. C. Evans and S. Clement, *Polym. Chem.*, 2014, **5**, 3352-3362.
30. A. Gutacker, N. Koenen, U. Scherf, S. Adamczyk, J. o. Pina, S. M. Fonseca, A. J. M. Valente, R. C. Evans, J. Seixas de Melo, H. D. Burrows and M. Knaapila, *Polymer*, 2010, **51**, 1898-1903.
31. A. Gutacker, S. Adamczyk, A. Helfer, L. E. Garner, R. C. Evans, S. M. Fonseca, M. Knaapila, G. C. Bazan, H. D. Burrows and U. Scherf, *J. Mater. Chem.*, 2010, **20**, 1423-1430.
32. G. Tu, H. Li, M. Forster, R. Heiderhoff, L. J. Balk, R. Sigel and U. Scherf, *Small*, 2007, **3**, 1001-1006.
33. J. Kesters, S. Govaerts, G. Pirotte, J. Drijkoningen, M. Chevrier, N. Van den Brande, X. Liu, M. Fahlman, B. Van Mele, L. Lutsen, D. Vanderzande, J. Manca, S. Clément, E. Von Hauff and W. Maes, *ACS Appl. Mater. Interfaces*, 2016, **8**, 6309-6314.
34. Y. Shi, L. Tan, L. Chen and Y. Chen, *Journal of Materials Chemistry C*, 2014, **2**, 8054-8064.
35. M. Chevrier, J. E. Houston, J. Kesters, N. Van den Brande, A. E. Terry, S. Richeter, A. Mehdi, O. Coulembier, P. Dubois, R. Lazzaroni, B. Van Mele, W. Maes, R. C. Evans and S. Clement, *J. Mater. Chem. A*, 2015, **3**, 23905-23916.
36. K. Yao, L. Chen, Y. Chen, F. Li and P. Wang, *J. Mater. Chem.*, 2011, **21**, 13780-13784.
37. X. Chen, L. Chen, K. Yao and Y. Chen, *ACS Appl. Mater. Interfaces*, 2013, **5**, 8321-8328.
38. Y. Kim, S. Cook, S. M. Tuladhar, S. A. Choulis, J. Nelson, J. R. Durrant, D. D. C. Bradley, M. Giles, I. McCulloch, C.-S. Ha and M. Ree, *Nat. Mater.*, 2006, **5**, 197-203.
39. J. E. Houston, S. Richeter, S. Clément and R. C. Evans, *Polym. Inter.*, 2017, **66**, 1333-1348.
40. E. Lee, B. Hammer, J.-K. Kim, Z. Page, T. Emrick and R. C. Hayward, *J. Am. Chem. Soc.*, 2011, **133**, 10390-10393.
41. T. Ghooos, N. Van den Brande, M. Defour, J. Brassinne, C.-A. Fustin, J.-F. Gohy, S. Hoepfner, U. S. Schubert, W. Vanormelingen, L. Lutsen, D. J. Vanderzande, B. Van Mele and W. Maes, *Eur. Polym. J.*, 2014, **53**, 206-214.
42. J. Rubio-Magnieto, A. Thomas, S. Richeter, A. Mehdi, P. Dubois, R. Lazzaroni, S. Clement and M. Surin, *Chem. Commun.*, 2013, **49**, 5483-5485.
43. R. K. Heenan, J. Penfold and S. M. King, *J. Appl. Crystallogr.*, 1997, **30**, 1140-1147.
44. www.mantidproject.org
45. G. D. Wignall and F. S. Bates, *J. Appl. Crystallogr.*, 1987, **20**, 28-40.
46. A. Guinier and G. Fournet, *Small Angle Scattering of X-rays*, John Wiley and Sons, 1955.
47. A. A. Golosova, J. Adelsberger, A. Sepe, M. A. Niedermeier, P. Lindner, S. S. Funari, R. Jordan and C. M. Papadakis, *J. Phys. Chem. C*, 2012, **116**, 15765-15774.
48. F. Nallet, R. Laversanne and D. Roux, *J. Phys. II France*, 1993, **3**, 487-502.
49. J. Berghausen, J. Zipfel, P. Lindner and W. Richtering, *J. Phys. Chem. B*, 2001, **105**, 11081-11088.
50. I. Livsey, *J. Chem. Soc. Faraday Trans.*, 1987, **83**, 1445-1452.
51. www.sasview.org
52. K. K. Stokes, K. Heuzé and R. D. McCullough, *Macromolecules*, 2003, **36**, 7114-7118.
53. K. Faied, M. Frechette, M. Ranger, L. Mazerolle, I. Levesque, M. Leclerc, T.-A. Chen and R. D. Rieke, *Chem. Mater.*, 1995, **7**, 1390-1396.
54. Y.-H. Lee, W.-C. Yen, W.-F. Su and C.-A. Dai, *Soft Matter*, 2011, **7**, 10429-10442.

55. M. Sundberg, O. Inganäs, S. Stafström, G. Gustafsson and B. Sjögren, *Solid State Commun.*, 1989, **71**, 435-439.
56. V. M. Sadtler, F. Giulieri, M. P. Krafft and J. G. Riess, *Chem. Eur. J.*, 1998, **4**, 1952-1956.
57. P. D. T. Huibers, *Langmuir*, 1999, **15**, 7546-7550.
58. M. Isamu, T. Akira, Y. Masakatsu and K. Hiroshi, *Bull. Chem. Soc. Jpn*, 1990, **63**, 3502-3507.
59. P. Mukerjee and K. J. Mysels, *Critical Micelle Concentration of Aqueous Surfactant Systems*, National Bureau of Standards Washington, DC, 1970.
60. SANS measurements performed on each of the surfactants in deuterated-methanol (conc. = [10 mg mL⁻¹]) suggested that no micelles were formed at this concentration (see Fig. S5, ESI[†]).
61. Q. Yuan, R. Ravikrishna and K. T. Valsaraj, *Sep. Purif. Technol.*, 2001, **24**, 309-318.
62. L. Nordstierna, I. Furó and P. Stilbs, *J. Am. Chem. Soc.*, 2006, **128**, 6704-6712.
63. H. G. Kim, B. Kang, H. Ko, J. Lee, J. Shin and K. Cho, *Chem. Mater.*, 2015, **27**, 829-838.
64. S. Dai, F. Zhao, Q. Zhang, T.-K. Lau, T. Li, K. Liu, Q. Ling, C. Wang, X. Lu, W. You and X. Zhan, *J. Am. Chem. Soc.*, 2017, **139**, 1336-1343.
65. T. J. Prosa, M. J. Winokur, J. Moulton, P. Smith and A. J. Heeger, *Macromolecules*, 1992, **25**, 4364-4372.
66. M. Chevrier, J. E. Houston, J. Kesters, N. Van den Brande, A. E. Terry, S. Richeter, A. Mehdi, O. Coulembier, P. Dubois, R. Lazzaroni, B. Van Mele, W. Maes, R. C. Evans and S. Clement, *J. Mater. Chem. A*, 2015, **3**, 23905-23916.
67. J. B. Hayter and J. Penfold, *Mol. Phys.*, 1981, **42**, 109-118.
68. J.-P. Hansen and J. B. Hayter, *Mol. Phys.*, 1982, **46**, 651-656.
69. J. B. Hayter and J. Penfold, *Colloid Polym. Sci.*, 1983, **261**, 1022-1030.
70. B. Hammouda, *J. Appl. Crystallogr.*, 2010, **43**, 716-719.
71. P. Kélicheff, C. Grabielle-Madelmont and M. Ollivon, *J. Colloid Interface Sci.*, 1989, **131**, 112-132.
72. N. A. Mazer, G. B. Benedek and M. C. Carey, *J. Phys. Chem.*, 1976, **80**, 1075-1085.
73. P. W. Schmidt, *Some Fundamental Concepts and Techniques Useful in Small-Angle Scattering Studies of Disordered Solids. In Modern Aspects of Small-Angle Scattering*, Kluwer Academic Publishers: Dordrecht, The Netherlands, 1995.
74. M. J. M. Wirix, P. H. H. Bomans, H. Friedrich, N. A. J. M. Sommerdijk and G. de With, *Nano Lett.*, 2014, **14**, 2033-2038.
75. D. Yu, M. Tian, Y. Fan, G. Ji and Y. Wang, *J. Phys. Chem. B*, 2012, **116**, 6425-6430.
76. Silicon wafers were cleaned before sample deposition with Piranha solution (3:1 mixture of conc. sulfuric acid and hydrogen peroxide) to remove organic residue.
77. A. González-Pérez, J. M. Ruso, G. Prieto and F. Sarmiento, *J. Surfactants Deterg.*, 2004, **7**, 387-395.
78. H. Erothu, J. Kolomanska, P. Johnston, S. Schumann, D. Deribew, D. T. Toolan, A. Gregori, C. Dagron-Lartigau, G. Portale and W. Bras, *Macromolecules*, 2015, **48**, 2107-2117.
79. R. Noriega, J. Rivnay, K. Vandewal, F. P. V. Koch, N. Stingelin, P. Smith, M. F. Toney and A. Salleo, *Nat. Mater.*, 2013, **12**, 1038-1044.
80. S. Y. Son, Y. Kim, J. Lee, G.-Y. Lee, W.-T. Park, Y.-Y. Noh, C. E. Park and T. Park, *J. Am. Chem. Soc.*, 2016, **138**, 8096-8103.